IEEE Journal of Microwaves

Received 10 August 2023; revised 17 September 2023 and 18 October 2023; accepted 19 October 2023. Date of publication 13 November 2023; date of current version 8 January 2024.

Digital Object Identifier 10.1109/JMW.2023.3327188

A UAV Based CMOS Ku-Band Metasurface FMCW Radar System for Low-Altitude Snowpack Sensing

ADRIAN TANG [1,2] (Senior Member, IEEE), NACER CHAHAT [1] (Fellow, IEEE), YANGYHO KIM [3] (Senior Member, IEEE), ARHISON BHARATHAN [2] (Student Member, IEEE), GABRIEL VIRBILA [2], HANS-PETER MARSHALL [4], THOMAS VAN DER WEIDE [4], GAURANGI GUPTA [1] (Member, IEEE), RAUNIKA ANAND [1,2], GOUTAM CHATTOPADHYAY [1] (Fellow, IEEE), AND MAU-CHUNG FRANK CHANG [2] (Life Fellow, IEEE)

(Invited Paper)

[1]Jet Propulsion Laboratory, California Institute of Technology, Pasadena, CA 91106 USA
[2]University of California, Los Angeles, CA 90095 USA
[3]Stevens Institute of Technology, Hoboken, NJ 07030 USA
[4]Boise State University, Boise, ID 83725 USA

CORRESPONDING AUTHOR: Adrian Tang (e-mail: ajtang@jpl.nasa.gov).

This work was supported by NASA Earth Science Technology Office Award through NASA Instrument Incubator Program under Grant 80NM0020F0032. Part of this paper was carried out at the Jet Propulsion Laboratory, California Institute of Technology, under a contract with the National Aeronautics and Space Administration (80NM0018D0004).

ABSTRACT This article presents development of a UAV based frequency modulated continuous wave (FMCW) radar system for remotely sensing the water contained within snowpacks. To make the radar system compatible with the payload requirements of small UAV platforms, the radar electronics are implemented with CMOS technology, and the antenna is implemented as an extremely compact and lightweight metasurface (MTS) antenna. This article will discuss how the high absorption losses of snowpacks lead to dynamic range requirements much stricter than FMCW radars used for automotive and other sensing applications, and how these requirements are met through antenna isolation, leakage calibration and exploitation of the range correlation effect. The article discusses in detail the implementation of the radar system, the CMOS microwave and digital circuitry, and the MTS antenna. The developed radar was mounted on a drone and conducted surveys in both Idaho and Alaska during the 2022-2023 winter season. We present several of those field results.

INDEX TERMS MetaSurface, CMOS radar, FMCW radar, snowpack, remote sensing, UAV.

I. NEED FOR REMOTE SENSING OF SNOW, FOR WATER RESOURCE AVAILABILITY AND PLANNING AND CHALLENGES OF REMOTE SENSING OF SNOW

The Southwestern United States has long been known for its arid climate and challenging water supply, but the impacts of climate change have intensified these issues significantly in recent decades. The region is experiencing a disturbing phenomenon known as a "megadrought" [1], [2], [3], [4], a prolonged and severe drought that has stretched across several years, threatening water resources and ecosystems. One of the key drivers of this megadrought is the loss of snowpack in the Sierra Mountains, which has far-reaching implications for water availability in the Colorado River Basin [5], [6], [7], [8]. The Sierra Nevada Mountains have traditionally acted as a vital water reservoir for the Southwest, capturing winter precipitation as snowpack, which gradually melts and replenishes rivers and streams during the warmer months. However, rising temperatures due to climate change have disrupted this delicate balance. A recent study by the California Water Resource Board [9] revealed that the Sierra snowpack has diminished

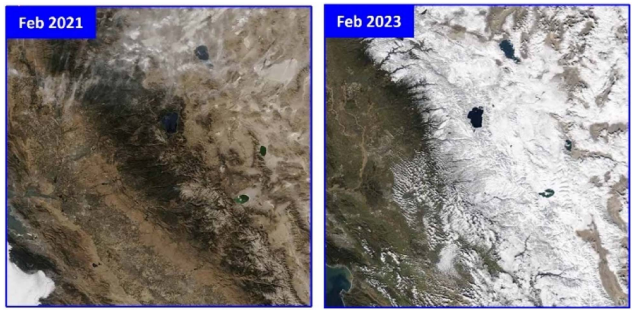

FIGURE 1. Snowpack in the Sierra Nevada Mountain range in a drought year (2021) and a non-drought year (2023).

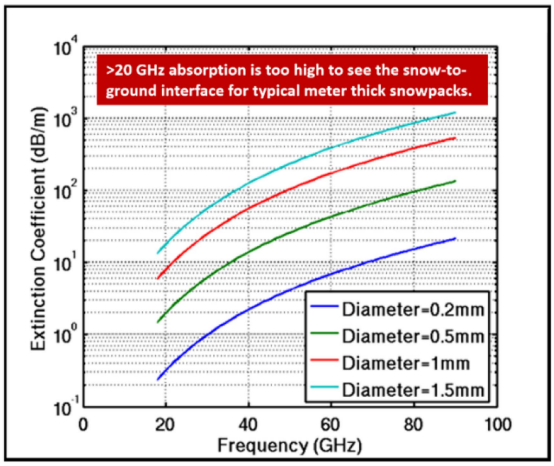

FIGURE 2. Microwave absorption of a dry snowpack vs. frequency for grain sizes (snowflake sizes) ranging from 0.2 mm to 1.5 mm from [11].

by nearly 30% over the past century. The impact of declining snowpack is particularly pronounced in the Colorado River Basin, one of the most critical water sources for the region. Reduced snowmelt from the Sierras has contributed to declining water levels in the Colorado River, leading to water shortages for major metropolitan areas including Sacramento, Los Angeles, and San Diego as well as agricultural regions like the San Joaquin valley. Fig. 1 shows the Sierra Mountains during a drought year (2021) compared with a more typical snowpack (2023) showing considerable reduction in the snow and ultimately water resources available from the mountain range for human use.

One key part element of effective planning and water resource use through careful measurement of the water each year, and allocation to the various stakeholders (municipalities, agriculture, industry). As this must be done in the winter season, the primary form of water will be snowpacks, and so a need exists to remotely determine how much water will be produced from a given snowpack after it melts and replenishes its river systems and associated reservoirs. To accomplish this measurement, we have developed a UAV based snow radar system to support these water resource efforts. The presented FMCW radar operates over snowpacks and directly senses snow depth while providing the basis for also retrieving density information about the snowpack through model fitting. These measurements, while not able to retrieve snow-water equivalence (SWE) stand-alone provide important depth and coverage constraints for global observations like those in [10], [11] as part of an overall retrieval process.

Although in-situ sensing of snow is a mature field with many techniques available [12], remote sensing of the snowpack remains an elusive measurement where no single technique can produce a robust estimate of water content under all conditions. Several thorough studies of the remote sensing of snow have been completed Instead, a multi-sensor approach across multiple platforms (in-situ, airborne, spaceborne) is needed where data from the more localized and higher XY resolution in-situ measurements are used to constrain the spaceborne measurements that although much poorer in XY resolution, provide global coverage [10], [11]. While in the past these in-situ measurements were performed manually with a measuring stick on either robotic platforms or with humans exploring the snowpack, the coverage is poor due to travel in remote areas, and the measurement process is intensive at each site, leading to a very limited number of measurements available to constrain the global spaceborne data. To address this, we have developed a UAV-based frequency modulated continuous wave (FMCW) radar platform that takes the place of these in-situ measurements, still providing localized and targeted depth estimates of the snowpack, but over a larger area with many more measurement points, and in a far more automated fashion than is possible manually.

Prior Effort towards in-situ measurements: Several prior efforts exist in remote sensing of snow with radar from in-situ drone platforms [13], [14], [15], [16] for high resolution in situ surveys. [17], [18], [19] are also examples of radar sensing of snow but from much higher altitudes and less applicable to localized in-situ measurements. These examples are much low-resolution global surveys compared to high-resolution in-situ measurements of the snowpack. References [13], [14], [15] as mentioned target in-situ measurements offer the best comparison to the presented Ku band system (shown in Table 1). [13] demonstrated measurements at C-band using an ultra-wideband (UWB) approach at very low altitudes that was able to resolve shallow snowpacks in the 3–5 GHz range with synthetic aperture processing applied. A similar radar with comparable bandwidth was demonstrated in [15]. While these radars function well to capture both snow surfaces and snow ground interfaces at nadir, their longer wavelength limits XY resolution and localization of the radar beam even at low altitudes. Ref. [14] demonstrated results with an X-band radar that although offered improved spatial resolution exhibited a limited dynamic range as the radar was shown to detect snow-air and snow-ground interfaces quite well but struggled to see internal layering. Several other airborne (high altitude >1000 m approaches) to measuring snow have also been explored with full size aircraft as part of NASA's SnowEx campaign [20] but do not offer resolution or detailed structure in their radar echoes that these in-situ efforts do. Finally, we note that signal of opportunity approaches [21], [22] where reflections of other communication signals are used to

TABLE 1. Comparison of Recent Snow Radars for UAV Sensing

Parameter	[13]	[14]	[15]	[This work]
Radar Center Frequency	4.3 GHz	7.7 GHz	2.2 GHz	15 GHz
Bandwidth	2 GHz	1.3 GHz	3.8 GHz	1.4 GHz
Transmit Power	3 dBm	10 dBm	17 dBm	29 dBm
DC Power	Not Listed	Not Listed	9W	8.9W
SNDR	Not Listed	Not Listed	Not Listed	>90 dB (lab measured)
XY Resolution (at 10m altitude)*	42.1 m	23.7m	83.2 m	11. 8 m

*Assuming the same antenna size as our demonstration.

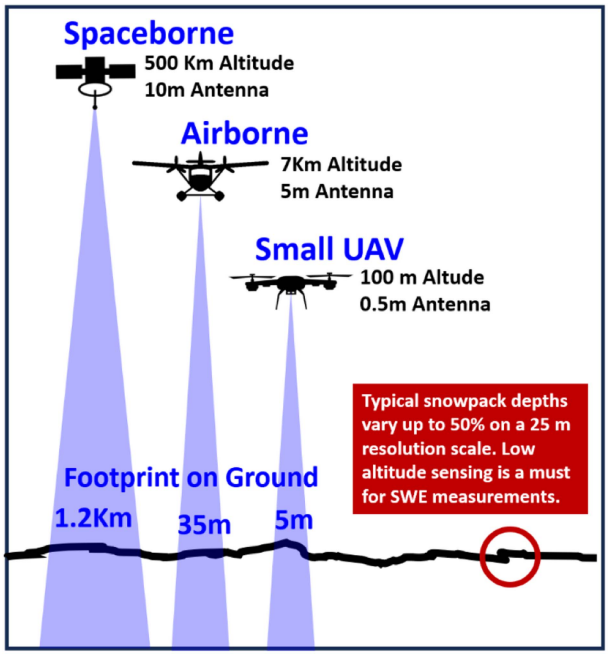

FIGURE 3. Attainable resolutions from space, airborne and drone platforms showing the attainable XY resolution on the ground for a Ku band radar. In typical snowpacks, SWE varies significantly at scales on the order of 25 m in the XY direction, highlighting the need for UAV sensing.

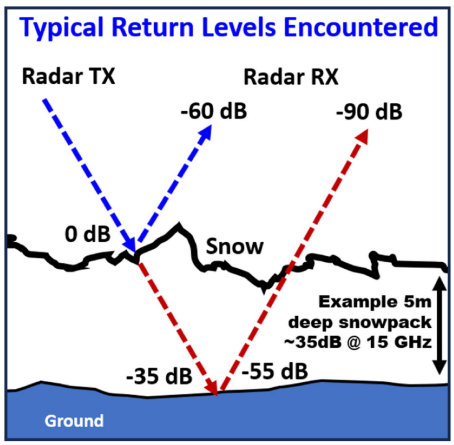

FIGURE 4. Typical radar return power levels relative to transmit power for a typical snowpack and the system.

interrogate the snowpack from Earth orbit have been explored for low resolution global surveys.

In this work we leverage the excellent work done in these prior in-situ snow sensing existing approaches and make several important changes. First, we implement our radar at Ku band (15 GHz) instead of the prior work at X or C band (1–8 GHz). This allows improved XY resolution as the radar beam experiences less diffraction with a given antenna size. Second, we implement the radar with a custom CMOS chip for the RF electronics and DSP greatly simplifying the radar implementation as all the radar components are within a single chip. Third we use oversampling of the radar's baseband waveform to improve radar dynamic range. Finally, we introduce a new type of antenna, metsurface antennas which are more compact and lightweight than antennas with comparable gain and similar wavelengths [23].

II. OVERVEIW OF RADAR SYSTEM LEVEL DESIGN

Frequency Selection for snow sensing: One of the first considerations is the optimal frequency or frequencies to sense the snowpack at. To retrieve depth of a snowpack, penetration up to considerable depths (possibly 5–10 m in the Sierras and similar mountain ranges) is required. Fig. 2 shows the extinction (absorption) curves for microwave frequencies with varying grain (snowflake) sizes. As you depart Ku-band, the microwave absorption becomes nearly unworkable for these thicker snowpacks, and both depth and density information can be lost. At the same time in Fig. 3, we show that for a low frequency radar the XY resolution on the ground becomes much poorer due to diffraction when a practical antenna size is considered. Snowpacks generally vary in water content on a XY resolution scale of about 25m [11] meaning that sensing with km-scale footprints is unable to produce robust localized estimates of SWE for constraining low XY-resolution global data. Ultimately an in-situ snow radar needs to trade-off higher-frequency for lower diffraction and improved XY resolution with lower-frequencies to be able to penetrate the deep snowpacks involved in water re source planning.

Dynamic range for snow sensing: Even with optimal frequency selection, detection of the snow-ground interface used to retrieve depth is not trivial due to the high dynamic range requirements. Fig. 4 shows an example link budget for a typical deep snowpack encountered during one of our campaigns, assuming 5m of snow depth with a typical distribution of snowflake sizes.

TABLE 2. Dynamic Range Analysis of the Proposed Radar

Parameter	Value
DAC SNDR	46 dB
DAC SNDR Floor (3 GS/s)*	-137 dBc / Hz
Chirp Time**	20 us
Detection Bandwidth (B_d)	50 KHz
DAC SNDR Floor integrated over detection bandwidth	-90 dBc
Noise inflation by PLL multiplication (n = 128)	42 dB
DAC SNDR floor at TX out	-48 dBc
Required TX to RX isolation for 20 dB SNR***	>62 dB

* Assumes SNDR is uniform across Nyquist bandwidth
** Fixed by ADC sample rate and demodulated FMCW bandwidth
*** Assumes integrated phase noise over B_d is lower than SNDR. (True with RCE)

Note that these link budget values can be scaled by the data in Fig. 2 to estimate the losses and signal powers at other wavelengths. Working through the level power diagram (see Table 2), we can determine the signal to noise plus distortion (SNDR) (a measure of dynamic range) needed for snowpack detection with a robust SNR. We first receive a reflection off the snowpack surface. As the dielectric constant of dry snow is very close to free space, this reflection is quite weak, typically in the −60 dB range (relative to transmitted power). The signal then penetrates 5m of snow incurring about 35 dB loss for typical dry snow, followed by up to a 20 dB loss worst-case in reflection at the snow-ground interface depending on surface topography. The reflected signal then incurs a second 35 dB loss as it exits the snowpack, arriving at the radar 90 dB down relative to the transmitted power. Unlike automotive radars or ground-penetrating radars (GPR) where targets of interest are bright (−40 to −60 dB typical range), the snow-ground interface is extraordinarily weak (−90 dB) and places extraordinary isolation requirements on a continuous wave (CW) radar between the transmitter and receiver. The concern here is that the broadband distortions leaking from the transmitter (notably phase noise and DAC quantization noise) to the receiver create an artificial detection floor far above the thermal noise floor of the receiver itself, limiting detection of these extraordinarily weak reflections. One novel approach in the proposed radar to improve SNDR is that although the FMCW chirp has relatively small bandwidth range prior to being multiplied up to Ku-band (55–66 MHz) and only requires a modest 120 MS/s of Nyquist sampling, we instead employ a high-speed DAC and oversample the FMCW waveform substantially at 3 GS/s. This oversampling allows the DAC (SNDR of 46 dB) to spread this distortion and quantization noise across its full 1.5 GHz Nyquist bandwidth instead of a narrow bandwidth at critical sampling, leading to a distortion floor of −137 dBc/Hz relative to the radar chirp assuming the distortion is uniformly distributed. For comparison this would be 10 log(1500/66) = 13.5 dB poorer SNDR if only the Nyquist bandwidth was used for FMCW waveform representation. The radar has a 20us chirp time giving a detection bandwidth of 50 KHz, and within that 50 KHz, the contribution of this DAC distortion will be −90 dBc relative to the radar chirp. In the radar this digital chirp is further multiplied up to Ku band (15.0–16.0 GHz) inflating these distortions to a final level of −42 dBc. Thus, to detect a −90 dB reflection with a 10 dB signal-to-noise (SNR), an isolation between TX and RX of at least 58 dB is required. Phase noise although a higher power spectral density at the receiver input than the SNDR distortion, benefits from the range correlation effect discussed in the next section and is ultimately suppressed to a level where the DAC distortions remain the limiting factor in detection. Also note these numbers are for a typical snowpack, and in extreme depths or with wet snow that becomes more absorbing, even the proposed radar can struggle to obtain robust detection of the snow-ground interface for SWE retrievals. For this demonstration with an extraordinary 60-65 dB of transmit to receive antenna isolation and 29 dBm of transmit power, the DAC SNDR broadband distortion level sits at −95 dBm relative to transmit power, while the thermal noise of the receiver with its 1.5 dB noise figure in the same detection bandwidth sits at −126 dBm meaning that distortion limits detection over thermal noise by over 30 dB.

Range correlation effect in short range radars: Similarly, phase noise is a broadband distortion that also would normally limit detectivity if it was not for the range correlation effect (RCE). The range correlation effect is a consequence of the radar transmitter and receiver sharing the same LO (and thus having the same instantaneous phase noise at transmitter and receiver) [24]. As a result, the phase noise of the transmitter is partially subtracted by the receiver although not entirely as there is some decorrelation due to the delay difference between the transmitted waveform that experiences the time-of-flight and the receiver that does not. Fig. 5 provides an overview of this effect where the time domain phasor for instantaneous phase noise is added at the transmitter, time delayed by the time of flight, then subtracted at the receiver. By taking the Fourier transform of this subtraction we can represent this partially correlated cancellation as a frequency domain linear time invariant (LTI) filter that has the shown magnitude and phase response. What we see is that phase noise at short range (the case in TX to RX leakage) is well suppressed out to several MHz by more than 20–30 dB. With the synthesizer's base phase noise of approx. −94 dBc/Hz at 50 KHz offset (see Fig. 11 later for this value), then integrated over the 50 KHz detection bandwidth of the

III. RADAR ELECTRONICS ARCHITECTURE

FMCW range bin width, gives a phase noise power spectral density of −47 dBc/bin, comparable the level of the DAC SNDR distortion level (−48 dBc/bin). This −47 dBc/bin of phase noise then incurs the range correlation advantage of at least 25 dB (from Fig. 5 assuming the TX to RX leakage path in the radar is under 10 m long) resulting in a final phase noise density of below −72 dBc/bin, well below the −48 dBc/bin of

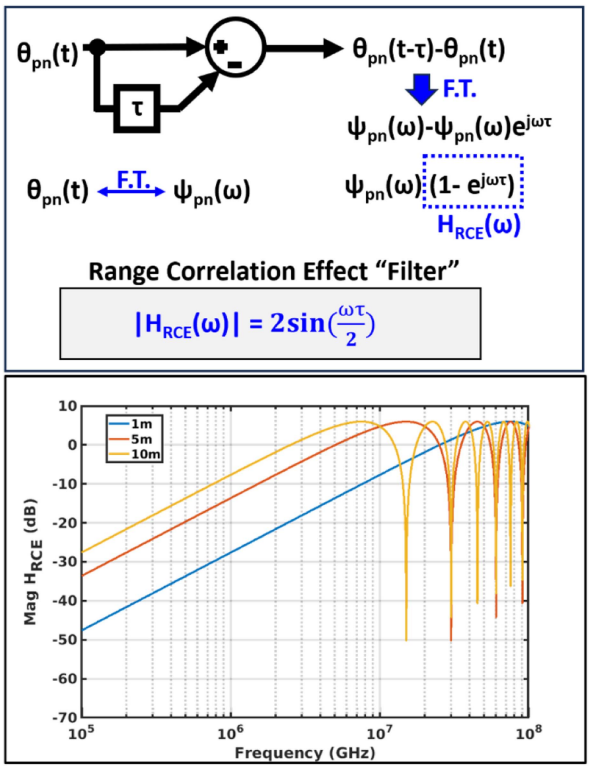

FIGURE 5. Range correlation effect where the same LO drives both transmitter and receiver leading to partial phase noise cancellation that can be represented as an LTI filter applied to system phase noise.

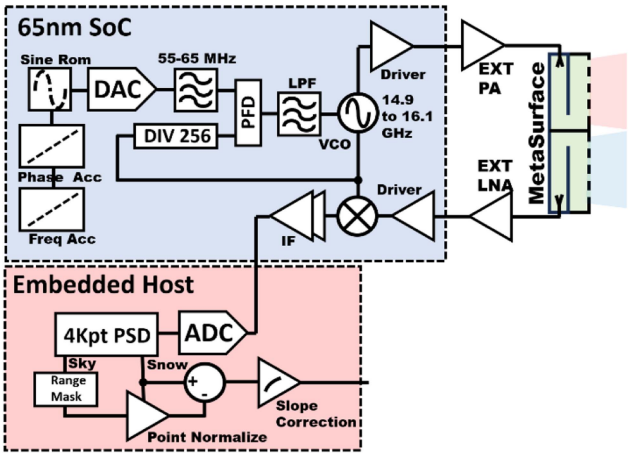

FIGURE 6. Block diagram of the Ku-radar system developed for snow sensing showing internal blocks of the 65 nm transceiver chip and external components with metasurface antenna.

the DAC SNDR distortion, meaning that the transmit SNDR is limiting detection of weak reflections to a level approximately 24 dB higher than the phase noise and confirming that it is indeed SNDR, not phase noise that ultimately limits the detection sensitive of the radar.

The Ku band radar system block diagram is shown in Fig. 6 and has evolved from our previous work reported in [23] that employed a much poorer performing ring voltage controlled

TABLE 3. Radar System Parameters

Parameter	Value
Radar Band	14.9 to 16.1 GHz
FMCW Chirp Bandwidth (b)	1.2 GHz
Chirp Time	20 us
FFT Bin / Detection Bandwidth	50 KHz
Range Resolution (Nominal c/2b)	12.5 cm
Transmit Power	29 dBm
Receiver Noise Figure	2 dB
DAC Physical Bits	10 bit
ADC Physical Bits	14 bits

oscillator (VCO) instead the LC-VCO based phase-locked-loop (PLL) in this work. The majority of the radar system is implemented in a single 65 nm CMOS chip with an integrated waveform generator, transmitter, receiver, and Ku-band frequency synthesizer, with the only components external to the chip being an embedded host computer to compute the FFT for the FMCW demodulation, and microwave amplifiers for the final transmit stage and first receive stage. The radar uses a compact and well isolated dual beam metasurface antenna [15] to provide high radar gain to maintain excellent XY resolution on the ground while still providing excellent TX to RX isolation. The radar waveform is generated by a chirping direct digital frequency synthesizer (DDFS) and on-chip DAC that produces a 58.2 to 62.89 MHz chirp which is then used as a reference for an on chip PLL that further multiplies the chirp frequency by a factor of 256. Although the radar output band of 14.9 to 16.1 GHz (1.2 GHz bandwidth) only requires a chirp occupying 58.2 to 62.89 MHz from the DDFS+DAC to be fed into the PLL prior to multiplication to Ku-band, we still operate the DAC at a full 3 GS/s so that the quantization noise is further spread across a full 1.5 GHz bandwidth instead of only over a narrow range of output frequencies, providing an oversampling advantage as mentioned in the previous Section. A 55–65 MHz bandpass filter then placed between the DAC and PLL so that most of this broadband distortion is rejected before being passed to the PLL loop. Finally post FMCW de-ramping in the CMOS chip, an embedded computer with a 14-bit ADC samples the IF signal synchronously, performs a 4K point FFT computation, and applies a sliding point normalized calibration with a slope correction adjustment. This calibration scheme is discussed later in Section VII. Table 3 lists the top-level parameters for the Ku-band radar system's chirp waveform and RF front-end performance.

IV. CIRCUIT LEVEL IMPLEMENTATION

Chirp Generator: The digital block diagram of the chirp generator is shown in Fig. 8 and uses two cascaded 17-bit accumulators to generate the chirp phase function. The first accumulator accumulates frequency at a constant programmed rate between two input frequency endpoints while the phase accumulator's rate is determined by the first frequency accumulator's output. This provides the second order phase function required for an FMCW frequency chirp. Finally, that

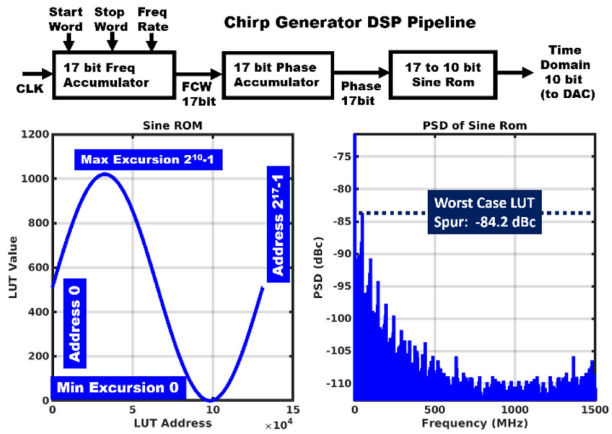

FIGURE 7. Block diagram of digital chirp generator and the sine-rom waveform seen in time domain, and in frequency domain.

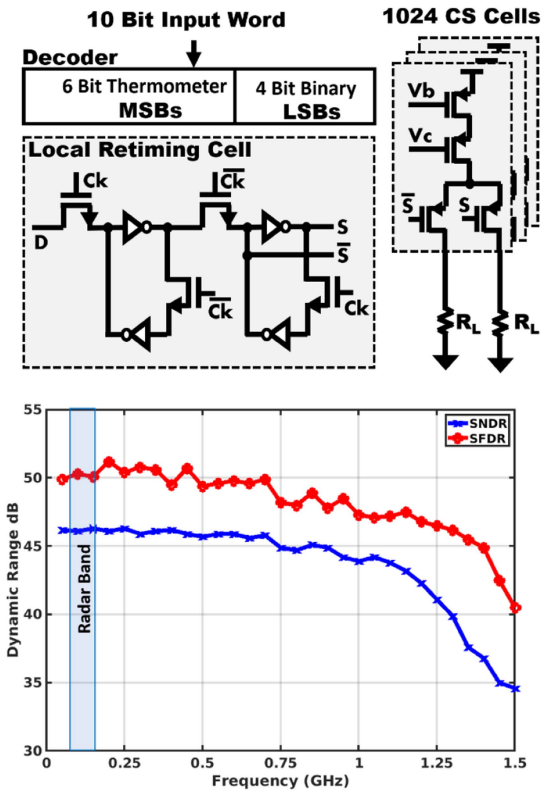

FIGURE 8. Current-steering DAC implementation and SNDR/SFDR vs frequency for a single tone output from near-DC to Nyquist showing the operating band in the radar system.

output 17-bit phase is converted to a 10-bit amplitude value via a sine ROM (a look up table of phase-in to voltage-out). In Fig. 7 we show the values in this look-up sine-ROM table and its limiting values of both the address and amplitude scale. In Fig. 8, we also show the discrete Fourier transform (DFT) of the sine-ROM values which show the spurs resulting from the discretization and phase-binning of the sine function result in spurs no worse than −84 dBc, indicating that the far higher power −48 dBc/bin distortion and quantization noise of the

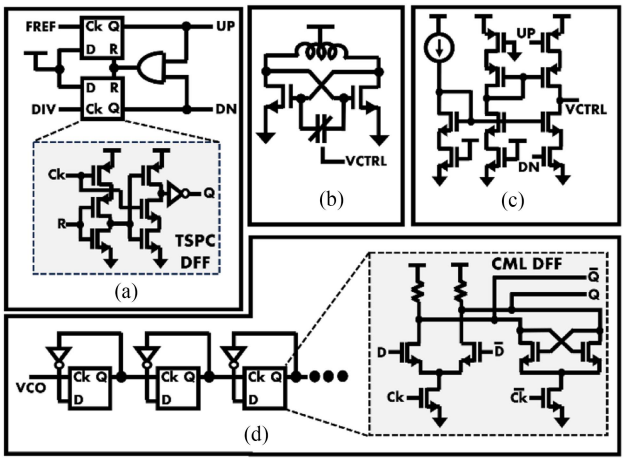

FIGURE 9. Key building blocks of the on-chip Ku synthesizer. (a) Phase detector schematic using TSPC latches. (b) VCO schematic. (c) Charge pump schematic. (d) Divider chain schematic using CML devices.

DAC itself will limit the radar's dynamic range, as opposed to these look-up table distortions.

The DAC itself is implemented as a current steering DAC and is a variant of the one presented in [25] with an improved retiming stage to allow higher sample rates. The DAC decoder is implemented as a segmented architecture as shown in Fig. 8 with the upper 6 bits being implemented with binary decoding and the lower 4 bits being implemented with thermometer decoding. Each local DAC cell has a double-cascaded latch implemented with pass-gates for improved dynamic performance and to reduce output glitching during code transitions. The current cells themselves are implemented as a PMOS cascode structure with a common bias and PMOS steering switches. The cell is stacked 1024 times (for 10 bits) and fed to a common set of differential resistors to provide the final I-to-V conversion at the output. The DAC is operated with a single tone to produce the measurement in Fig. 9 showing the spur-free dynamic range (SFDR) and signal to noise distortion ratio (SNDR) as a single output tone is varied from near DC frequencies up to the DAC's Nyquist frequency. Also marked on this plot is the 58.2 to 62.89 MHz bandwidth the FMCW chirp occupies at the DAC output during radar operation. Note as SNDR considers the spur energy for a DAC it should, by definition, be lower than the SFDR value under all conditions.

Ku-Band Synthesizer / Phase-Locked-Loop: The Ku-band synthesizer is implemented as an integer-n phase-locked loop using an LC-VCO. Fig. 9 shows the key circuit schematics within the synthesizer. The phase/frequency detector (PFD) is implemented as a reset-race circuit that produces up and down signals for the proceeding charge pump. As both the digital divider and input reference are single-ended, we use true-single phase clocked (TSPC) latches to implement the flipflops. The charge-pump itself is implemented with a cascode current mirror with switching devices to asymmetrically steer the current away from the output node. The VCO itself is implemented as an NMOS cross-coupled pair with a single differential inductor and varactor for frequency control. The divider chain

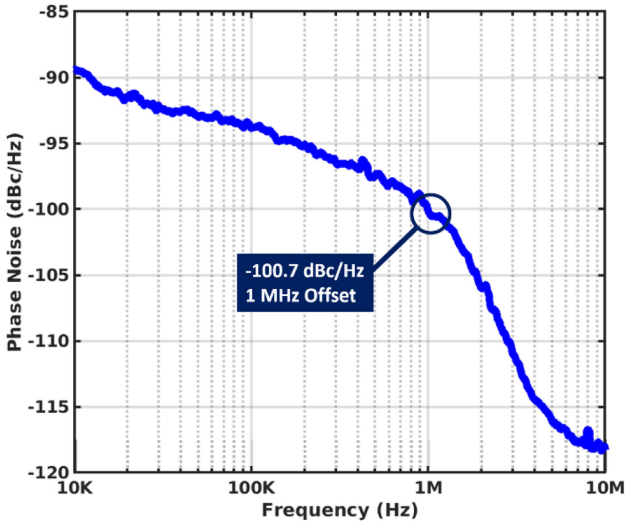

FIGURE 10. Measured phase noise of the Ku synthesizer when operated at a continuous frequency of 15.5 GHz (not chirped).

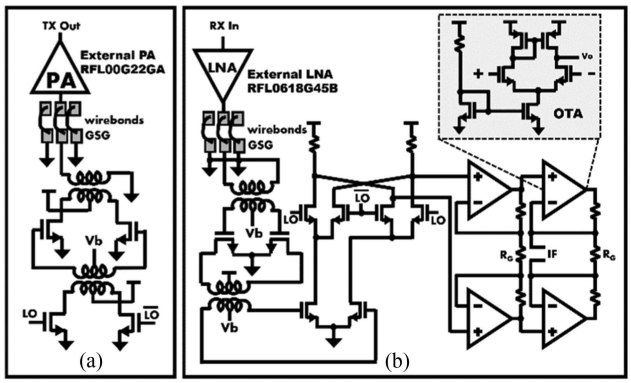

FIGURE 11. (a) Transmitter chain schematic. (b) Receiver chain schematic which uses CMOS closed loop OTAs for the IF stages. In both chains the external off-chip LNA and PA part numbers are provided.

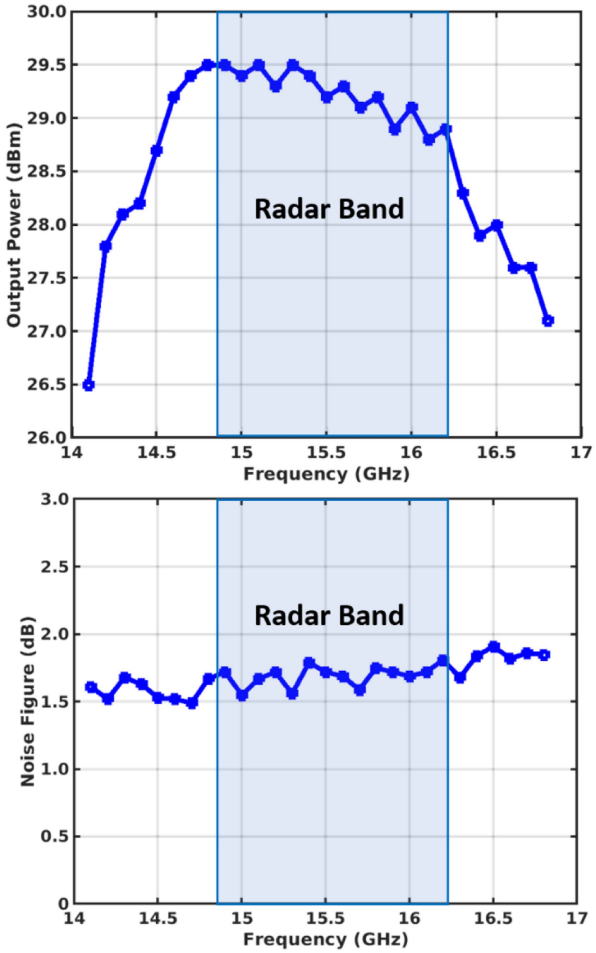

FIGURE 12. Measured transmit power and measured receiver noise figure. The radar chirp bandwidth is marked on each plot.

is implemented as an integer-n power-of-2 architecture where the divider flipflops are implemented with current-mode logic (CML) to support robust operation at 14.9–16.1 GHz, with a final swing restoring CMOS flop as the last divider stage. Fig. 10 shows the measured phase noise of the synthesizer when chirping operation is suspended and it is allowed to dwell mid-band at 15.5 GHz.

Transmitter and Receiver: The Ku-band transmitter and receiver have their schematic diagrams shown in Fig. 11. The transmitter chain uses a two-stage transformer-coupled differential common source amplifier, where gate and drain biasing are provided at the center-taps of the transformer networks. As the center-tap of the differential circuit is an AC null, this shields the impedance of the bias network from visibility at microwave frequencies and eliminates the need for bias-tee and DC blocking structures. After the final driver stage of the on-chip transmitter, the output signal is wirebonded to the PCB carrying a microstrip, and fed into an external GaAS amplifier (PN RFL00G22GA) [26] via an SMA connector which provides 29 dBm of transmit power to the radar antenna. The receiver is implemented similarly with an off-chip connectorized HEMT LNA as the first stage (PN RFL0618G45B) [27] to provide an extremely competitive noise figure. The LNA then feeds an on-chip driver/buffer circuit again implemented as a transformer coupled common source, and then drives a Gilbert double-balanced mixer which provides both down-conversion and FMCW deramping in a single stage as the reference chirp is applied to the LO port. Once de-ramped the radar waveform becomes quite narrowband (<10 MHz) compared to the Ku-band chirp signal, and so final IF amplification is provided by a cascade of on-chip operational transconductance amplifier (OTA) stages prior to being fed to the embedded computer with integrated ADC. Fig. 12 shows the transmitter and receiver performance at Ku-band highlighting the portion of the frequency band that the FMCW radar chirp occupies. Note that no configuration change was made between these lab measurements and the later outdoor surveys so these our best estimates of actual transceiver performance during the performed snow measurements. Fig. 13 shows the entire 65 nm radar system-on-chip with the key blocks (Tx, Rx, Chirp Gen,

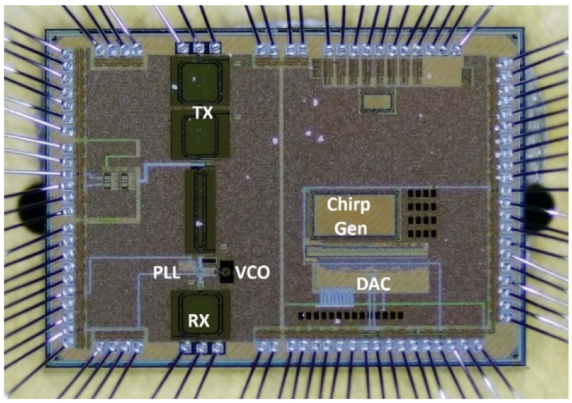

FIGURE 13. Die photo of the custom CMOS chip showing the key blocks of the Ku-radar system.

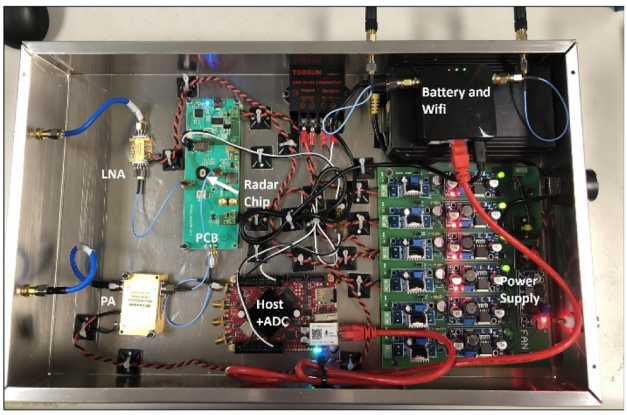

FIGURE 14. Integrated radar electronics into the UAV payload showing key components.

DAC, and PLL) identified in the photograph. The entire chip consumes 175 mW of DC power from a 1.0V power supply. Fig. 14 shows how the radar chip PCB is packaged into the larger radar module with all the key components labelled. The LNA and PA are connectorized and mounted separate of the radar PCB carrying the 65 nm CMOS chip. The embedded host computer with ADC is also connectorized.

The reason for connectorization of key components as opposed to a higher level of integration is so they can easily be swapped if a component fails in the remote field test areas that the UAV operates in. While failures are not common, they have occurred, primarily on the embedded computer related to SD card failures in cold weather. Within the packaged radar there is a considerable amount of power supply filtering, again to prevent any spurs or switching noise from corrupting the radar IF bandwidth and further limiting the radar's dynamic range. As we have found UAV provided power tends to carry such spurs, the Ku radar was instead packaged with an internal battery pack to maintain the "cleanest" supply power possible. For accessibility we carry a mini-WiFi router for uploading and downloading data from the embedded host, however that transceiver remains off during radar operations

TABLE 4. Mass and Power of Radar Payload Components

Parameter	Mass	Power
Radar PCB + Chip	82 g	244 mW
Ext. LNA	18 g	303 mW
Ext. PA	24 g	4750mW
Embedded Computer	198 g	2870mW
Wifi Router	175 g	0 during flight
PSU	210 g	800mW overhead
Battery	578 g	-
Structure (Box/Fasteners)	320 g	-
MetaSurface Antenna	2051 g	-
Totals:	3.66 Kg	8.97 W

to prevent RFI interference with the radar as the 3rd harmonic of the 5.4–5.8 GHz 802.11 WiFi is quite close to our RF band. Table 4 gives a mass and power breakdown for the entire radar payload to provide the reader a sense of the overall form factor.

V. METASURFACE ANTENNA IMPLEMENTATION

As discussed in detail in Section II the extremely weak snow-ground interface signals demand extremely high TX to RX isolation. While a pair of offset high-gain Ku-band horn antennas could provide this isolation, their size would be prohibitive for use in a small UAV payload as they occupy considerable volume. Alternatively, a flat panel antenna which is much easier to accommodate on a UAV platform would be preferable, but traditional planar antennas provide very limited isolation, especially when offset by small distances. Instead, we include a metasurface antenna (reported in detail in [15]) which provides both the compact form factor of a planar antenna and the extremely high isolation needed for snow sensing. Fig. 15 shows a diagram of the metasurface structure which is constructed with two offset sub-antennas for transmit and receive.

The metasurface antenna has two planar levels: a lower level where a planar horn transmits a spherical wave and then an upper level that couples a planar wavefront to a modulated surface to produce the designed radiation pattern. To couple the two levels, the end of the metasurface contains a parabolic reflector that converts the incident spherical wave on the lower level into a plane wave on the upper level.

Despite containing two sub-antennas the metasurface is extremely lightweight (only 2.05 Kg) and provides the very high isolation required for snow sensing as shown in Fig. 17 where both the isolation and return losses are shown. The worst-case isolation achieved is 59.4 dBm within the bandwidth that the FMCW chirp occupies. The antenna is well matched over this bandwidth as the return loss trace in Fig. 16 indicates. The measured antenna gain is shown in Fig. 17 across both E and H plane of intercepts of one of the sub-antennas at the band center. Note both TX and RX sub-antennas are identical structures.

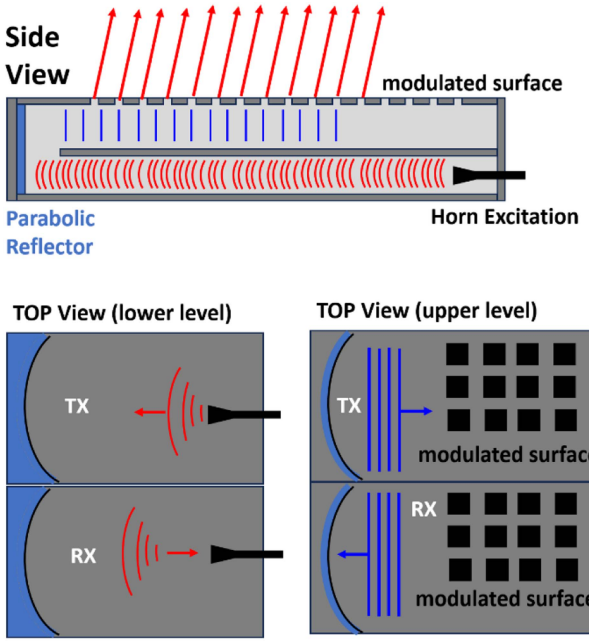

FIGURE 15. Diagram of the metasurface antenna showing the lower level where a parabolic reflector converts a spherical wave to a plane-wave and the top layer where a modulated surface provides the desired radiation pattern.

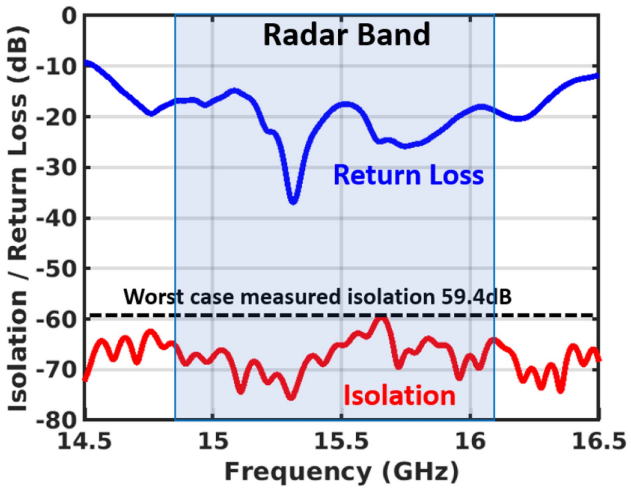

FIGURE 16. Measured return loss of each sub-antenna and isolation between sub-antennas with the radar chirp bandwidth indicated.

Also note that the beam angle in the H plane is not exactly boresight as the excitation of the metasurface creates a small angle. As the UAV radar only operates at low altitudes (<100 m) this beam angle is inconsequential to the XY resolution obtained at the snow surface. Fig. 18 shows a photograph of the entire metasurface antenna with transmit and receive sub-antennas identified as well as overall dimensions. One interesting feature of the metasurface antenna is that it is implemented entirely with metal containing no dielectric material at all, which is helpful when needing to operate at low temperatures. Connections to the antenna are provided by

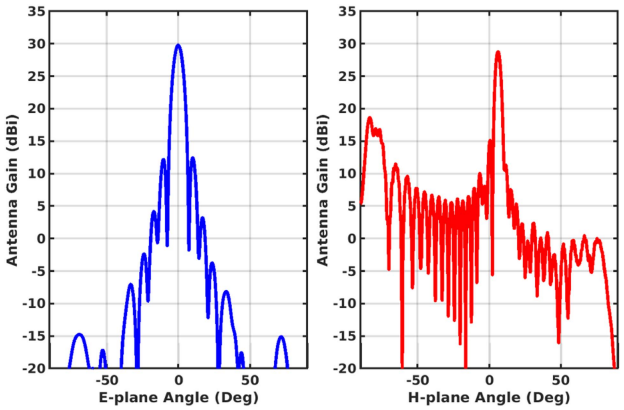

FIGURE 17. Measured E-plane and H-plane intercepts of one sub-antenna (both are identical) showing the measured gain at 15.5 GHz (band center).

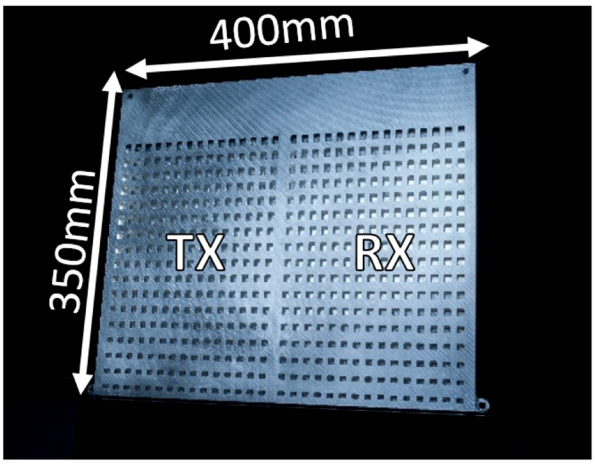

FIGURE 18. Photograph of metasuface antenna showing the separated transmitter and receiver sub-antennas, and overall dimensions.

two coax to horn transitions integrated into the back of the structure.

VI. CAMPAIGN AND AIRBORNE SNOW RESULTS

The Ku-band snow radar system has participated in several snow measuring campaigns during the 2022-2023 winter season. It first flew over several snowpacks near Boise Idaho, then in Grand Mesa Colorado, and finally over the snow-covered glaciers in Utqiagvik Alaska. Fig. 19 shows a heavy lift rotor drone during the Alaska campaign with the Ku radar payload and metasurface antenna mounted below during a long duration flight.

Raw Measurements and Calibration: Fig. 20(a) shows raw results collected during a 20-meter track over an approximately 40 cm deep snowpack. As the snowpack is quite thin the top (snow-air) and bottom (snow-ground) interfaces are comparable in intensity as the volume absorption is small. In the uncalibrated raw data of Fig. 20, one can see that the TX-RX leakage distortions continues to play a role, even with the high isolation delivered by the meta-surface antenna. Beyond leakage power from transmitter to receiver, several other

FIGURE 19. Ku-band radar mounted on a drone and operating long-range flights in Utqiagvik, Alaska.

artifacts exist that are also present including narrowband spurs coupling into the detection bandwidth from other electronics inside the radar enclosure (computer clock, interface clocks, and other RFI sources). As FMCW decodes into a periodic sine wave, any spur in the detection bandwidth appears like an echo at a constant range across the flight track. Additionally, some of these RFI sources like those from the computers or drive system of the UAV are intermittent non-CW signals and will not be continuous across the entire radar track although they will always occur at specific ranges as their frequencies do not change. Although the snow surface and snow-ground interface are somewhat visible in the raw data, there remains leakage and interference energy at other ranges making interpretation difficult and limiting the ability to determine a reliable snow depth estimate. Conventional GPR radar processing includes several key steps: first a range dependent gain called "gain recovery" is applied to equalize the added loss from penetrating deeper into the ground or snowpack [29], [30]. This is typically followed by position offset correction [31], [32], [33] that accommodates the air gap between the antenna and ground surface. Offsets are typically not an issue for snow sensing as we are only interested in the snow depth (top air-snow interface relative to bottom snow-ground interface), not the snow's position relative to the UAV. In our radar we do apply a uniform gain recovery, but then introduce a novel normalized sliding point calibration to address the intermittent signals. First, we capture the raw radar data by flying over the snowpack which is the data shown in Fig. 20(a). Each vertical column in this 2D plot in Fig. 20(a) represents one radar measurement in frequency domain $R_n(f)$ where the entire radar image can be expressed as simply the stacked set:

$$\mathrm{Rx(f)} = \{\mathrm{R_1(f)}, \mathrm{R_2(f)}, \ldots, \mathrm{R_n(f)}, \ldots, \mathrm{R_N(f)}\} \quad (1)$$

Where $R_N(f)$ corresponds to the radar frequency domain waveform at the 20 m position (end of the track). The next step is to place the radar on the ground upside down so the beam is pointed into the sky and no radar echo is present. This produces the data shown in Fig. 20(b) which captures the internal leakage of the radar as well as the interference spurs within the radar enclosure. Although the radar itself is not moving in this measurement step, we still use a 0–20 m scale on the X-axis so that the traces captured, and their indexes correspond to the time taken to travel that distance in the original radar plot. Note at the beginning of this trace there is some disturbance due to the person setting up the radar contacting the radar beam. This data is truncated before the calibration is used. This sky pointed step produces sky calibration data SK where each column again is a frequency domain radar trace $SK_n(f)$.

Therefore the entire skycal image can be expressed as:

$$\mathrm{SK(f)} = \{\mathrm{SK_1(f)}, \mathrm{SK_2(f)}, \ldots, \mathrm{SK_n(f)}, \ldots, \mathrm{SK_N(f)}\} \quad (2)$$

We then average the undisturbed part of the sky calibration (the red box of Fig. 17(b)) to produce an average skycal waveform A(f) where

$$A(f) = \frac{1}{N-m} \sum_{k=m}^{N} SK_k(\mathrm{f}). \quad (3)$$

This waveform A(f) expresses the average amount of leakage power on a per frequency that the radar captures from the transmitter to receiver as well as any interference internal to the radar package. However, upon inspection of the leakage signal present in Fig. 20(a)(the raw return) one can see the amount of leakage is not constant from radar trace to radar trace. As mentioned much of the interference can be time varying which explains why it is not constant at all points along the radar track. Regardless of source (interference or leakage mechanisms), the varying nature of the leakage signal within the raw returns during the flown track suggest that simply subtracting the average leakage A(f) from the raw returns will not adequately suppress the leakage power, and in fact may introduce artifacts at track positions where the leakage energy is lower than A(f). To address this, we perform the sliding point normalization shown in Fig. 20(c) where normalize A(f) by the total power of each radar trace in the original raw data Rx(f) to produce the sliding point calibration Cx(f) where

$$\mathrm{Cx(F)} = \{\mathrm{Cx1(f)}, \mathrm{Cx2(f)}, \ldots, \mathrm{Cxn(f)}, \ldots, \mathrm{CxN(f)}\} \quad (4)$$

and each radar trace $\mathrm{Cx}_n(f)$ in the sliding point function is computed as:

$$\mathrm{Cx}_n(\mathrm{f}) = \frac{A(f)}{\frac{1}{Y}\sum_{k=1}^{Y} R_n(\mathrm{k})} \quad (5)$$

Where Y is the total number of frequency domain points in each radar trace. By applying this correction, we essentially normalize the average leakage A(f) by the total power received by the radar at each point along the capture track. Finally, we can produce the final radar image F(f) shown in

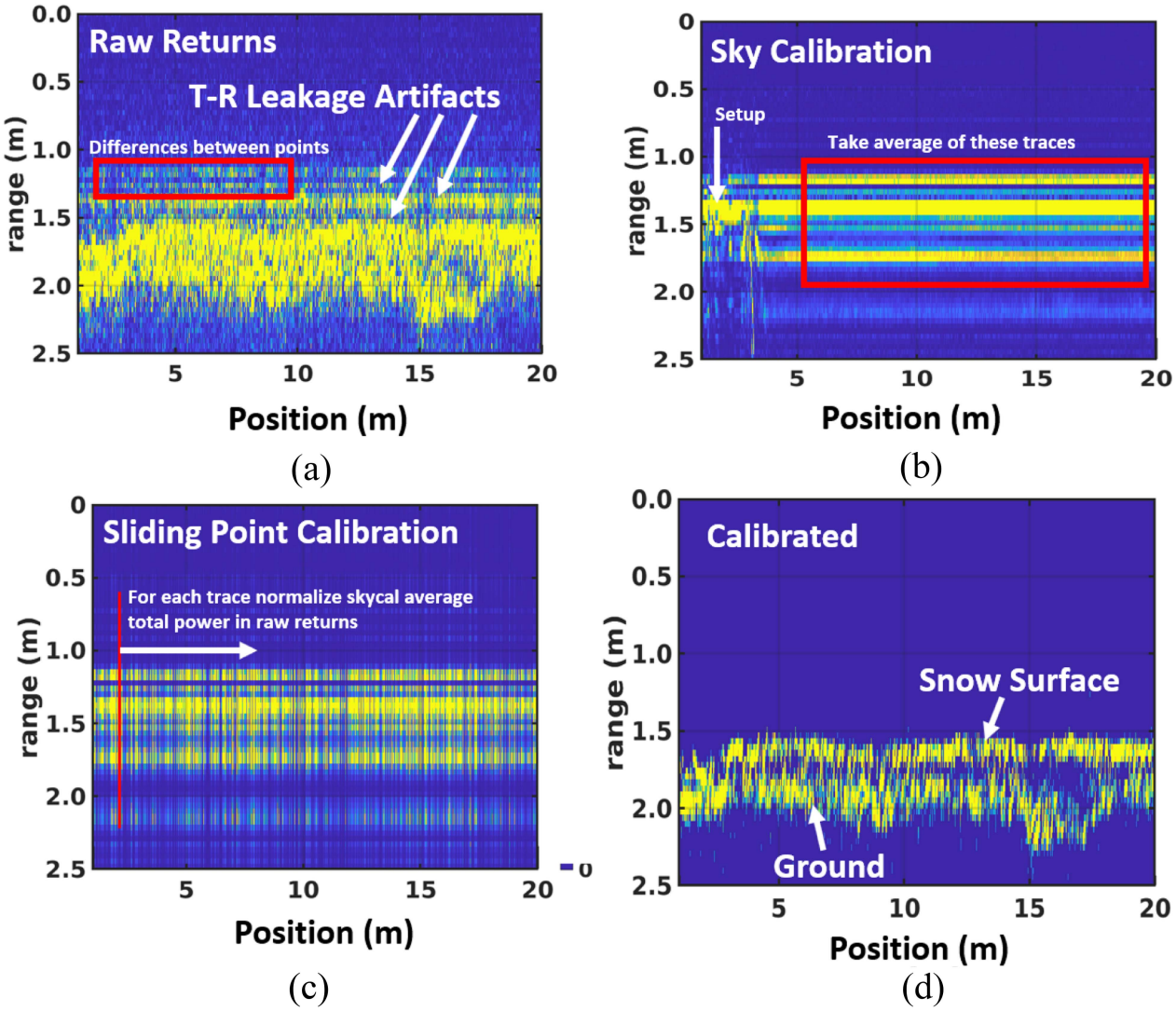

FIGURE 20. Radar captures from a 20 m track showing calibration process. (a) Uncalibrated raw radar data. (b) Sky calibration data. (c) Sliding point normalized calibration data. (d) Calibrated snow data.

Fig. 20(d), and defined as

$$F(f) = \{F_1(f), F_2(f), \ldots, F_n(f), \ldots, F_N(f)\} \quad (6)$$

where each radar trace in this final output track is computed as

$$F_n(f) = R_n(f) - Cx_n(f). \quad (7)$$

As one can see from the final output track in Fig. 20(d), the resulting calibrated data is obvious, and the snow-ground and snow surface interfaces are clearly visible. While offset correction is not required for snow depth estimates, the average wave velocity through the snowpack needs to be corrected to arrive at a correct depth. In this effort we employ the methodology outlined in [34] and leveraged our validation excavation values to inform the density parameters. Ultimately this density can be determined remotely from passive radiometer measurements co-located with the radar as described in [35]. The end-goal of this effort is to co-locate the presented Ku radar with the radiometer instrument already demonstrated in [36] for this purpose. Fig. 21 provides additional longer-range radar tracks taken in both shallow (~0.25 m) and deep (~3 m) snow conditions during the Idaho campaign in the Cat's Creek area (near Boise). Note that the range axis considers only the wave velocity in the snow, meaning that the absolute distance from the snow surface to the radar on the UAV is not valid. This is acceptable as for snowpack monitoring we are only concerned with the thickness of the snowpack itself and not the distance between the UAV and snow surface. Similarly, as the UAV changes altitude along the flown track (to avoid obstacles and changes in ground elevation), the absolute position of the snow changes relative to the UAV, however the depth of the snow which is the parameter we are interested in (the distance from the snow-air to snow-ground interfaces in the radargram) remains valid at all points along the track. In the deeper snow measurement, some interesting features are visible including a dark region over a creek where water has

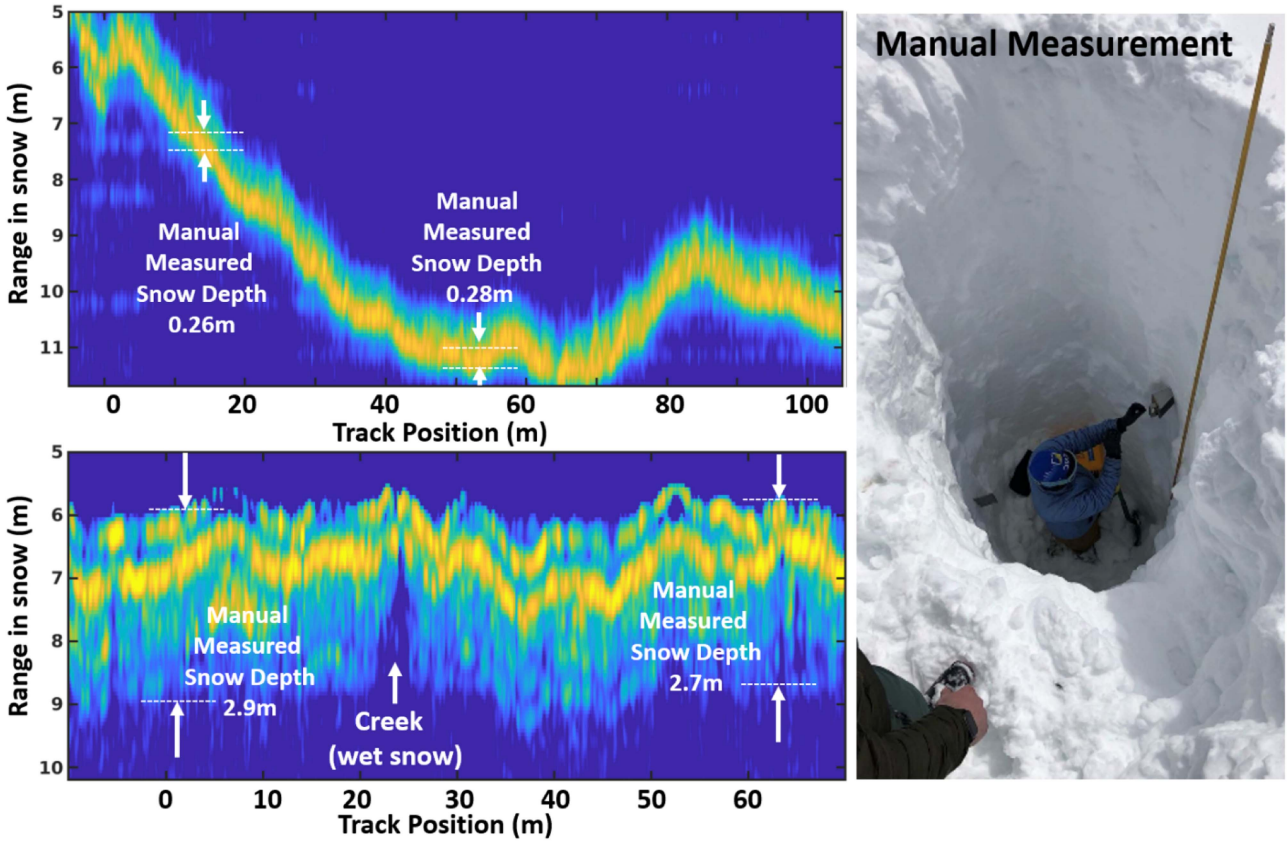

FIGURE 21. Examples of captured snow in both shallow snow (~0.25 m) and deep snow (~3 m) conditions compared to manual measurement with a measuring stick at two points along each flight track.

been drawn up into the snow making it far more absorbing, and an internal reflection in the middle of the snowpack where there is a snow-snow interface formed by two different snowfall events with considerably different grain sizes and densities. Finally for validation purposes we selected two points along the UAV's flown track (indicated by the red and black bars in the trace) and manually measured the snow depth and confirmed the snow was indeed completely dry. The smaller graphs in the right of Fig. 21 show the FMCW frequency domain outputs for the red and black marked positions along the track as well as a green line indicating the manually measured depth of snow with a ruler. From this validation we can see the Ku-band radar is quite capable of estimating snow depth as the peak returns from the interfaces correspond well to the measured depths.

VII. SUMMARY

In this article we first discuss the importance of monitoring water resources to respond to climate change, and the need for in-situ snowpack measurements to constrain globally collected spaceborne data. We discuss in detail the challenges related to the high absorption of typical snowpacks and how this imposes strict dynamic range requirements on an FMCW radar related to transmitter-to-receiver isolation. We show how through the range correlation effect, that phase noise is suppressed, and it is in fact the DAC SNDR distortions that ultimately limit radar sensitivity. We then describe in detail the implementation of a UAV Ku-band snow sensing radar reviewing both the system and circuit details for both the on-chip and off-chip blocks. We show how this radar was successfully integrated into a UAV payload and combined with a low-profile metasurface antenna that provides high isolation between transmitter and receiver. We present a technique for calibration that provides a robust enhancement of detection for both the snow surface, and snow-ground interfaces within a snowpack, allowing better access to depth and density estimates. Finally, we present example measurements from two recent campaigns in Idaho in both shallow and deep snowpack conditions to demonstrate the measurements attainable with the presented system.

ACKNOWLEDGMENT

The authors thank TSMC for their excellent 65 nm foundry support.

REFERENCES

[1] A. P. Williams et al., "Large contribution from anthropogenic warming to an emerging North American megadrought," *Science*, vol. 368, no. 6488, pp. 314–318, 2020.

[2] L. J. M. A. Pattanun and S. C. Anenberg, "Drought-sensitivity of fine dust in the US Southwest: Implications for air quality and public health under future climate change," *Environ. Res. Lett.*, vol. 13, no. 5, 2018, Art. no. 054025.

[3] P. R. Sheppard et al., "The climate of the US Southwest," *Climate Res.*, vol. 21, no. 3, pp. 219–238, 2002.

[4] W. Zhang, "The dry and hot American Southwest under the present and future climates," *Atmospheric Ocean. Sci. Lett.*, vol. 16, 2023, Art. no. 100340.

[5] L. Huizar et al., "Water supply in the Lower Colorado River Basin: Effectiveness of the 2019 drought contingency plan," *J. Environ. Eng.*, vol. 149, no. 10, 2023, Art. no. 04023058.

[6] B. Bass et al., "Aridification of Colorado River Basin's snowpack regions has driven water losses despite ameliorating effects of vegetation," *Water Resour. Res.*, vol. 59, no. 7, 2023, Art. no. e2022WR033454.

[7] A. Hernández-Cruz et al., "Assessing water management strategies under water scarcity in the Mexican portion of the Colorado River Basin," *J. Water Resour. Plan. Manage.*, vol. 149, no. 9, 2023, Art. no. 04023042.

[8] J. C. Schmidt, C. B. Yackulic, and E. Kuhn, "The Colorado River water crisis: Its origin and the future," *Wiley Interdiscipl. Rev., Water*, vol. 0, 2023, Art. no. 1672.

[9] "California Dept of Water Resources," in *California's Most Significant Droughts-Comparing Historical and Recent Conditions*. California Water Watch, 2020. [Online]. Available: https://cawaterlibrary.net/document/californias-mostsignificant-droughts-comparing-historical-and-recentconditions/

[10] J. M. Pflug et al., "Extending the utility of space-borne snow water equivalent observations over vegetated areas with data assimilation," *EGUsphere*, vol. 2023, pp. 1–26, 2023.

[11] W. G. Rees, *Remote Sensing of Snow and Ice*. Boca Raton, FL, USA: CRC Press, 2005.

[12] N. J. Kinar and J. W. Pomeroy, "Measurement of the physical properties of the snowpack," *Rev. Geophys.*, vol. 53, pp. 481–544, 2015.

[13] F. Abushakra et al., "Snow depth measurements with ultra-wideband compact FMCW radar on a small unmanned aircraft system," *IEEE J. Radio Freq. Identification*, vol. 7, pp. 343–351, 2023.

[14] K. G. Kjelgård and T. S. Lande, "Evaluation of UWB radar module for snow water equivalent monitoring," in *Proc. 52nd Eur. Microw. Conf.*, 2022, pp. 87–90, doi: 10.23919/EuMC54642.2022.9924383.

[15] R. Jenssen, R. Ole, and S. Jacobsen, "Drone-mounted UWB snow radar: Technical improvements and field results," *J. Electromagn. Waves Appl.*, vol. 34, no. 14, pp. 1930–1954, 2020.

[16] S. Prager, G. Sexstone, D. McGrath, J. Fulton, and M. Moghaddam, "Snow depth retrieval with an autonomous UAV-mounted software-defined radar," *IEEE Trans. Geosci. Remote Sens.*, vol. 60, 2022, Art. no. 5104816.

[17] H. Machguth, O. Eisen, F. Paul, and M. Hoelzle, "Strong spatial variability of snow accumulation observed with helicopter-borne GPR on two adjacent Alpine glaciers," *Geophys. Res. Lett.*, vol. 33, 2006, Art. no. L13503.

[18] J. St. Clair and W. S. Holbrook, "Measuring snow water equivalent from common-offset GPR records through migration velocity analysis," *Cryosphere*, vol. 11, pp. 2997–3009, 2017.

[19] T. Guneriussen, K. A. Hogda, H. Johnsen, and I. Lauknes, "InSAR for estimation of changes in snow water equivalent of dry snow," *IEEE Trans. Geosci. Remote Sens.*, vol. 39, no. 10, pp. 2101–2108, Oct. 2001, doi: 10.1109/36.957273.

[20] E. Kim et al., "NASA's SnowEx campaign: Observing seasonal snow in a forested environment," in *Proc. IEEE Int. Geosci. Remote Sens. Symp.*, 2017, pp. 1388–1390.

[21] C. C. Lin et al., "Active microwave scattering signature of snowpack—Continuous multiyear SnowScat observation experiments," *IEEE J. Sel. Topics Appl. Earth Observ. Remote Sens.*, vol. 9, no. 8, pp. 3849–3869, Aug. 2016, doi: 10.1109/JSTARS.2016.2560168.

[22] F. Koch et al., "Retrieval of snow water equivalent, liquid water content, and snow height of dry and wet snow by combining GPS signal attenuation and time delay," *Water Resour. Res.*, vol. 55, pp. 4465–4487, 2019.

[23] G. Gupta, A. Tang, and N. Chahat, "Ku-band metal-only flat metasurface radar antenna for small platforms," in *Proc. IEEE Antennas Propag. Soc. Symp.*, 2023.

[24] P. Tschapek, G. Körner, C. Carlowitz, and M. Vossiek, "Detailed analysis and modeling of phase noise and systematic phase distortions in FMCW radar systems," *IEEE J. Microwaves*, vol. 2, no. 4, pp. 648–659, Oct. 2022, doi: 10.1109/JMW.2022.3195574.

[25] Y. Kim, A. Tang, K.-N. Liou, T. H. Painter, and M.-C. F. Chang, "A ku-band CMOS FMCW radar transceiver for snowpack remote sensing," *IEEE Trans. Microw. Theory Techn.*, vol. 66, no. 5, pp. 2480–2494, May 2018, doi: 10.1109/TMTT.2018.2799866.

[26] S. D'Souza, F. Hsiao, A. Tang, S.-W. Tam, R. Berenguer, and M.-C. F. Chang, "A 10-bit 2-GS/s DAC-DDFS-IQ-controller baseband enabling a self-healing 60-GHz radio-on-chip," *IEEE Trans. Circuits Syst. II, Exp. Briefs*, vol. 60, no. 8, pp. 457–461, Aug. 2013.

[27] [Online]. Available: https://www.rflambda.com/pdf/poweramplifier/RFLUPA00G22GA.pdf

[28] [Online]. Available: https://www.rflambda.com/pdf/lownoiseamplifier/RLNA0618G45B.pdf

[29] N. Economou et al., "GPR data processing techniques," in *Civil Engineering Applications of Ground Penetrating Radar*. Berlin, Germany: Springer, 2015, pp. 281–297.

[30] S. C. Fisher, R. R. Stewart, and H. M. Jol, "Processing ground penetrating radar (GPR) data," *CREWES Res. Rep.*, vol. 4, pp. 1–20, 1992.

[31] M. van der Merwe and I. J. Gupta, "A novel signal processing technique for clutter reduction in GPR measurements of small, shallow land mines," *IEEE Trans. Geosci. Remote Sens.*, vol. 38, no. 6, pp. 2627–2637, Nov. 2000.

[32] J.-H. Kim, S.-J. Cho, and M.-J. Yi, "Removal of ringing noise in GPR data by signal processing," *Geosciences J.*, vol. 11, pp. 75–81, 2007.

[33] V. Santos, N. Rafael, and F. L. Teixeira, "Application of time-reversal-based processing techniques to enhance detection of GPR targets," *J. Appl. Geophys.*, vol. 146, pp. 80–94, 2017.

[34] H.-P. Marshall, G. Koh, and R. R. Forster, "Estimating alpine snowpack properties using FMCW radar," *Ann. Glaciol.*, vol. 40, pp. 157–162, 2005.

[35] T. Koike and T. Suhama, "Passive-microwave remote sensing of snow," *Ann. Glaciol.*, vol. 18, pp. 305–308, 1993.

[36] A. Tang, Y. Kim, and M.-C. F. Chang, "A fully-integrated CMOS system-on-chip ku band radiometer system for remote sensing of snow and ice," in *Proc. IEEE/MTT-S Int. Microw. Symp.*, 2022, pp. 1006–1008.